*Publ. Astron. Soc. Japan* (2021) 73 (1), 205–219
doi: 10.1093/pasj/psaa115
Advance Access Publication Date: 2021 January 13

# ALMA view of the Galactic super star cluster RCW 38 at 270 au resolution

**Kazufumi Torii**,[1] **Kazuki Tokuda**,[2,3,*] **Kengo Tachihara**,[4] **Toshikazu Onishi**,[2] **and Yasuo Fukui**[4,5]

[1]Nobeyama Radio Observatory, National Astronomical Observatory of Japan (NAOJ), National Institutes of Natural Sciences (NINS), 462-2, Nobeyama, Minamimaki, Minamisaku, Nagano 384-1305, Japan
[2]Department of Physical Science, Graduate School of Science, Osaka Prefecture University, 1-1 Gakuen-cho, Naka-ku, Sakai, Osaka 599-8531, Japan
[3]National Astronomical Observatory of Japan, National Institutes of Natural Science, 2-21-1 Osawa, Mitaka, Tokyo 181-8588, Japan
[4]Graduate School of Science, Nagoya University, Chikusa-ku, Nagoya, Aichi 464-8601, Japan
[5]Institute for Advanced Research, Nagoya University, Furo-cho, Chikusa-ku, Nagoya, Aichi 464-8601, Japan

*E-mail: tokuda@p.s.osakafu-u.ac.jp

Received 2019 July 17; Accepted 2020 December 7

## Abstract

We report millimeter/submillimeter continuum and molecular line observations of the Galactic super star cluster RCW 38, obtained from the Atacama Large Millimeter/Submillimeter Array with a minimum angular resolution of 0.″17 × 0.″15 (≃ 289 au × 255 au). The $C^{18}O$ image reveals many massive condensations embedded within filamentary structures extending along the northwest–southeast direction in the center of cluster. The condensations have sizes of 0.01–0.02 pc, $H_2$ column densities of $10^{23}$–$10^{24}$ cm$^{-2}$, and $H_2$ masses of 10–130 $M_\odot$. In addition, the 233 GHz continuum image reveals two dense, small millimeter-sources with radii of 460 and 200 au (Source A and Source B). Source A is embedded within the most massive $C^{18}O$ condensation, whereas no counterpart is seen for Source B. The masses of Source A and Source B are estimated as 13 and 3 $M_\odot$ at the optically thin limit, respectively. The $C^{18}O$ emission shows a velocity gradient of 2 km s$^{-1}$ at the central 2000 au of Source A, which could be interpreted as a Keplerian rotation with a central mass of a few $M_\odot$ or infall motion of gas. Further, the ALMA $^{12}CO$ data reveal that Source A and Source B are associated with molecular outflows exhibiting maximum velocities of ∼30–70 km s$^{-1}$. The outflows have short dynamical timescales of <1000 yr and high-mass outflow rates of ∼$10^{-4}$–$10^{-3}$ $M_\odot$ yr$^{-1}$. These observational signatures suggest an early evolutionary phase of the massive star formation in Source A and Source B.

**Key words:** ISM: clouds — ISM: molecules — radio lines: ISM — stars: formation

## 1 Introduction

The formation mechanism of massive stars is not yet thoroughly understood. A number of theoretical models invoke a scaled-up version of the low-mass model, with a disk-like structure and jets or outflows (e.g., Krumholz et al. 2007, 2009, 2010; Hosokawa & Omukai 2009; Hosokawa et al. 2010; Kuiper et al. 2010, 2011; Kuiper & Hosokawa 2018; Peters et al. 2010). Otherwise,

massive young stellar objects (YSOs) could not accrete by overcoming the powerful radiation pressure of luminous protostars (e.g., Wolfire & Cassinelli 1986; Nakano 1989). Observations of jets and outflows associated with massive YSOs, which resemble those of low-mass YSOs, provide indirect evidence of high-mass accretion disks (Beuther et al. 2002; Maud et al. 2015). However, observations providing a 100 au-scale resolution of the structures of massive YSOs are scarce.

Interferometric observations with an angular resolution of a few hundred au can be anticipated to reveal fragmentation, collapse, and outflowing gas of hidden dense materials that lead to the protostar formation, as demonstrated by recent Atacama Large Millimeter/Submillimeter Array (ALMA) observations in nearby low- and high-mass star-forming regions (e.g., Tokuda et al. 2014, 2016, 2019b; Hirota et al. 2017; Ohashi et al. 2018; Caselli et al. 2019; Matsushita et al. 2019). Several interferometric centimeter-to-submillimeter studies of luminous massive YSOs have resulted in the discovery of rotating structures on the order of 100 to 1000 au (Sánchez-Monge et al. 2013; Guzmán et al. 2014; Johnston et al. 2015; Cesaroni et al. 2017; Beuther et al. 2017; Motogi et al. 2019). However, it is still crucial to study a greater number of massive YSOs resolved at the 100 to 1000 au scale.

In this paper, we report new observations of the Galactic super star cluster RCW 38, obtained using the ALMA cycle-3 capability. RCW 38 is an outstanding super star cluster located at 1.7 kpc, and harbors $\sim 10^4$ stars, including $\sim$20 O-type stars (and candidates) within a small region of a few parsecs (Wolk et al. 2006; Winston et al. 2011; Kuhn et al. 2015, see also a review by Wolk et al. 2008). Most importantly, RCW 38 is the youngest super star cluster reported in the Milky Way, with an age of only $\sim$0.1–0.5 Myr (Wolk et al. 2008; Fukui et al. 2016). Despite strong dissipative and destructive effects caused by feedback from the formed massive stars, plenty of molecular gas still remains within the central $\sim$1 pc of RCW 38, offering a unique opportunity to observe the natal gas of the super star cluster during formation (Fukui et al. 2016).

RCW 38 has two sources that are bright in the near-infrared. The brightest feature at 2 $\mu$m is known as IRS 2, an O5.5 binary located at the center of the cluster (DeRose et al. 2009), the luminosity of which was measured as $7 \times 10^5\,L_\odot$ (Furniss et al. 1975). Another bright feature, labeled IRS 1, is located 0.1 pc west of IRS 2; this feature is a dust ridge extending by 0.1–0.2 pc in the north–south direction. The central 0.1 pc of IRS 1 and IRS 2 is devoid of dust, with cavities evidenced by infrared and millimeter observations (Huchtmeier 1974; Vigil 2004; Wolk et al. 2006, 2008).

Based on molecular line observations acquired with single-dish millimeter and submillimeter telescopes, Fukui et al. (2016) claimed that the formation of O stars in RCW 38 was triggered by a collision between two molecular clouds. The two identified clouds have radial velocities of $\sim$2 and $\sim$12 km s$^{-1}$. The former, the "ring cloud," has a ring-like structure surrounding the cavities of IRS 1 and IRS 2, has a mass of $3 \times 10^4\,M_\odot$ and is the primary body of the natal cloud of RCW 38, whereas the latter, the "finger cloud," is elongated across the cluster and is less dense, with a mass of $2 \times 10^3\,M_\odot$. The two clouds are connected in velocity space by an intermediate velocity feature (called the "bridge feature"). The bridge feature is located at 0.3 pc north of IRS 1 and IRS 2, indicating that the collisional interaction still continues, as suggested by the cloud–cloud collision model (Torii et al. 2015, 2017a; Fukui et al. 2018). Izumi et al. (2021) observed these molecular clouds in the [C I] emission line, indicating that the abundance ratio of CO to C I is constant for visual extinction $A_v$ of a few mag to 100 mag. This result may be interpreted with the clumpy photodissociation region (PDR) model (e.g., Spaans & van Dishoeck 1997; Tachihara et al. 2018), in which clumpy structures with sizes of less than a few 0.1 pc are predicted in the molecular clouds.

The ALMA observations in RCW 38 (P.I.: Fukui, Y., #2015.1.01134.S) were conducted for the central 1.5 pc $\times$ 0.7 pc of IRS 1 and IRS 2 in ALMA band-6 and band-7, using the main 12 m array and the Atacama Compact Array (ACA). The minimum angular resolution of the dataset is $0\farcs17 \times 0\farcs15$, which corresponds to 289 $\times$ 255 au at 1.7 kpc. The sources are embedded within dense dust condensations and are associated with molecular outflows having high mass outflow rates, suggesting massive star formation. The remainder of this paper is organized as follows. Section 2 describes the ALMA dataset used in this study. Section 3 presents the main results obtained by analyzing the ALMA dataset. The results are discussed in section 4, and finally, a summary is presented in section 5.

## 2 Observations

The parameters of the ALMA observations are summarized in table 1, whereas the datasets used in this study are listed in table 2. The ALMA observations were conducted using the cycle-3 band-6 (1.3 mm) and band-7 (0.87 mm) capabilities. The band-6 observations were performed using the 12 m array and the ACA [the 7 m array and the Total Power (TP) array]. The target molecular lines were $^{12}$CO $J = 2$–1, $^{13}$CO $J = 2$–1, C$^{18}$O $J = 2$–1, SiO $J = 5$–4, and H30$\alpha$, with spectral resolutions set to 141 kHz ($\sim$0.18 km s$^{-1}$) or 244 kHz ($\sim$0.31 km s$^{-1}$). A baseband with a bandwidth of 1875 MHz centered on 233 GHz was used to obtain the

**Table 1.** Spectral parameters of the ALMA observations.

| Line/continuum | Band | Frequency (GHz) | Spectral resolution (kHz) | Array |
|---|---|---|---|---|
| Continuum | 6 | 233.000 | 31.250 (MHz) | 12 m, ACA |
| Continuum | 7 | 341.000 | 31.250 (MHz) | ACA |
| $^{12}$CO $J = 2$–1 | 6 | 230.538 | 141 | 12 m, ACA |
| $^{13}$CO $J = 2$–1 | 6 | 220.399 | 141 | 12 m, ACA |
| C$^{18}$O $J = 2$–1 | 6 | 219.560 | 141 | 12 m, ACA |
| SiO $v = 0$ $J = 5$–4 | 6 | 217.105 | 244 | 12 m, ACA |
| H30$\alpha$ | 6 | 231.901 | 141 | 12 m, ACA |
| $^{13}$CO $J = 3$–2 | 7 | 330.588 | 244 | ACA |
| C$^{18}$O $J = 3$–2 | 7 | 329.331 | 244 | ACA |
| CS $J = 7$–6 | 7 | 342.883 | 244 | ACA |

**Table 2.** List of the ALMA datasets used in this paper.

| Image | Array | Spectral resolution (km s$^{-1}$) | Beam ($''$) | Noise* (mJy beam$^{-1}$) | Name† |
|---|---|---|---|---|---|
| Continuum (233 GHz) | 12 m | ... | 0.17 × 0.15 | 0.45 | 233 GHz |
| $^{12}$CO $J = 2$–1 | 12 m | 1.0 | 0.50 × 0.49 | 4.3 | $^{12}$CO |
| C$^{18}$O $J = 2$–1 | 12 m | 0.5 | 0.23 × 0.21 | 19.6 | C$^{18}$O |
| H30$\alpha$ | 12 m | 2.0 | 0.23 × 0.20 | 8.2 | H30$\alpha$ |
| $^{13}$CO $J = 2$–1 | 12 m + ACA | 0.2 | 1.90 × 1.55 | 123.8 | $^{13}$CO$_{\rm all}$ |
| C$^{18}$O $J = 2$–1 | 12 m + ACA | 0.2 | 2.13 × 1.74 | 93.1 | C$^{18}$O$_{\rm all}$ |
| Continuum (233 GHz) | ACA | ... | 7.25 × 5.29 | 15.3 | 233 GHz$_{\rm ACA}$ |
| Continuum (341 GHz) | ACA | ... | 4.75 × 3.65 | 37.2 | 341 GHz$_{\rm ACA}$ |
| $^{12}$CO $J = 2$–1 | ACA | 0.25 | 7.3 × 5.2 | 167 | $^{12}$CO$_{\rm ACA}$ |
| C$^{18}$O $J = 3$–2 | ACA | 0.25 | 5.0 × 3.6 | 215 | C$^{18}$O$_{\rm ACA}$ |
| H30$\alpha$ | ACA | 0.25 | 7.2 × 5.3 | 150 | H30$\alpha_{\rm ACA}$ |

*The noise is given per channel for line data cubes.
†The shortened name of the dataset used in this paper.

continuum emission. The pointing numbers of the 12 m array with the C40-6 configuration and the 7 m array were 33 and 13, respectively. The projected baselines of the 12 m and 7 m array observations were 15–3247 m and 8–44 m, respectively. The bandpass, flux, and phase calibrators were J1107−4449, J1107−4449, and J0851−5228, respectively, in the 12 m array observations. With the 7 m array, they were J1058+0133, Callisto, and J0904−5735, respectively.

The band-7 observations, on the other hand, were carried out with the ACA alone. Three spectral windows were used to observe molecular lines of $^{13}$CO $J = 3$–2, C$^{18}$O $J = 3$–2, and CS $J = 7$–6 at a spectral resolution of 244 kHz (∼0.22 km s$^{-1}$), while the continuum emission was observed using a baseband with a bandwidth of 1875 MHz centered on 341 GHz. The pointing number of the mosaicing observation was 27. The projected baseline length of the 7 m array ranged from 8 to 44 m. We observed J1256−0547 or J0522−3627 as the bandpass calibrators, and J1256−0547 or J0522−3627 as the flux calibrators. The phase calibrator was J0845−5458 throughout the observations.

In this study, only the datasets of CO lines and continuum emission were used to investigate the several 100 to 1000 au-scale structures of RCW 38. Herein, individual datasets are denoted by the names listed in the "Name" column in table 2. The obtained data were reduced using the Common Astronomy Software Application (CASA) package (McMullin et al. 2007), whose version is 5.5.0. We used the `tclean` task using the Briggs weighting with a robust parameter of 0.5. In order to acquire better sensitivities, a uv-tapering was applied to the $^{12}$CO and C$^{18}$O$_{\rm all}$ data, which resulted in larger synthesized beams of ∼0.″5 and ∼2″, respectively. For the C$^{18}$O $J = 2$–1 emission, two data cubes with different beam sizes (C$^{18}$O$_{\rm all}$ and C$^{18}$O) were generated to illustrate the large-scale gas structures and the small-scale gas kinematics around compact mm-sources in RCW 38 (figures 1 and 4). Note that the 12 m array and 7 m data were combined together in visibility space to make the combined image, and then we used the `feathering` task in CASA to merge the 12 m + 7 m arrays and the TP data for the C$^{18}$O$_{\rm all}$ data.

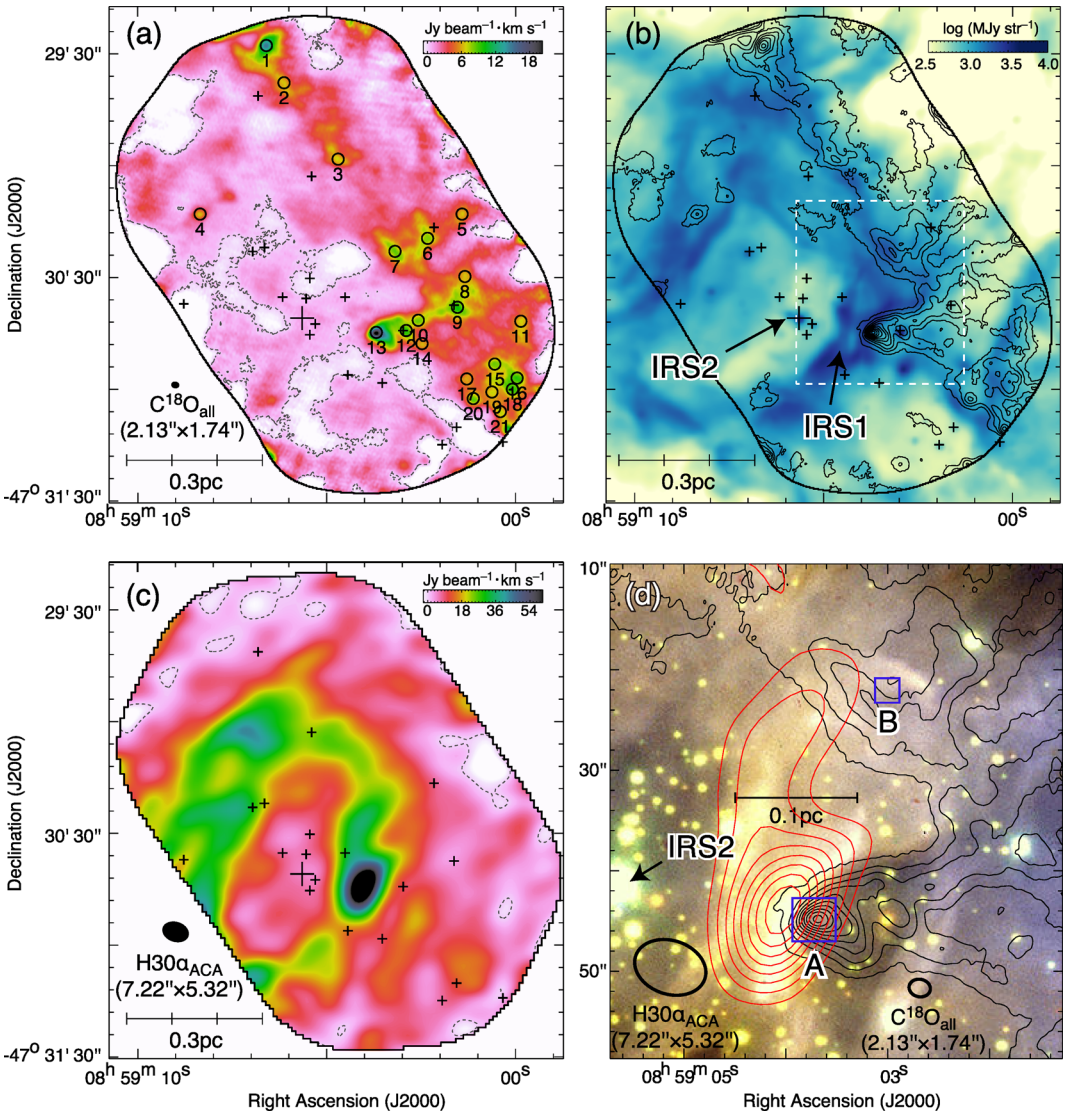


**Fig. 1.** (a) Intensity distributions of the $C^{18}O_{all}$ data integrated over a velocity range of $-2$–$+12\,km\,s^{-1}$. Dashed contours indicate the zero level of the $C^{18}O_{all}$ image. Circles indicate the positions of the $C^{18}O$ condensations. (b) Contour map of the $C^{18}O_{all}$ image in panel (a) superimposed on the Spitzer/IRAC 5.8 $\mu$m image (Wolk et al. 2008). Contours start at 1 Jy beam$^{-1}$ km s$^{-1}$ with steps of 2 Jy beam$^{-1}$ km s$^{-1}$. (c) H30$\alpha_{ACA}$ image, with the dashed contours plotted at the zero level. The velocity integration range is from $-20$ to 30 km s$^{-1}$. In panels (a), (b), and (c), the large cross indicates the central O5.5 star IRS 2, whereas small crosses indicate the O star candidates (Winston et al. 2011). (d) VLT near-infrared $J$ (blue), $H$ (green), and $K_s$ (red) images (Wolk et al. 2006) shown in the region indicated by the white box in panel (b). Black contours show the $C^{18}O_{all}$ distribution plotted in panel (b), whereas H30$\alpha_{ACA}$ is shown in the red contours starting at 10$\sigma$ (23 Jy beam$^{-1}$ km s$^{-1}$) with steps of 3$\sigma$ (6 Jy beam$^{-1}$ km s$^{-1}$). The two boxes marked by blue lines indicate the regions of Source A and Source B shown in figures 3a and 3b, respectively.

## 3 Results

### 3.1 Large-scale $C^{18}O$ distribution

From the $C^{18}O_{all}$ data with a resolution of $\sim$2″, figures 1a and 1b show the $C^{18}O$ intensity distribution integrated over $-2$ to $+14\,km\,s^{-1}$, which covers the velocity ranges of the ring cloud, finger cloud, and bridge feature. The majority of the emission arises from the ring cloud. The $C^{18}O_{all}$ map shows filamentary structures with widths of 0.1–0.2 pc, extending along the northwest–southeast direction, the rim of which at the bottom side is illuminated by nearby O stars, as indicated by the bright 5.8 $\mu$m emission (figure 1b). The filamentary structures include many condensations. The condensations were identified from the $C^{18}O_{all}$ integrated intensity map in figure 1a using the "clumpfind" algorithm (Williams et al. 1994), where the lowest detection level was set to 5$\sigma$ (=3 Jy beam$^{-1}$ km s$^{-1}$). Distributions of the 21 identified condensations are indicated by the circles in figure 1a, whereas their physical properties are summarized in table 3.

**Table 3.** Physical properties of the $C^{18}O$ condensations.

| # | RA (J2000.0) | Dec (J2000.0) | $r$ (pc)/(au) | $\sigma_v$* (km s$^{-1}$) | Peak $N_{H_2}$ ($\times10^{23}$ cm$^{-2}$) | $M_{H_2}$ ($M_\odot$) | $n_{H_2}$† ($\times10^7$ cm$^{-3}$) | $M_{vir}$ ($M_\odot$) |
|---|---|---|---|---|---|---|---|---|
| 1 | $8^h59^m06\overset{s}{.}60$ | −47°29′27″.7 | 0.021/4370 | 1.1 | 5.5–5.6 | 28–34 | 1.1–1.3 | 28 |
| 2 | $8^h59^m06\overset{s}{.}13$ | −47°29′37″.7 | 0.019/4010 | 1.2 | 2.4–2.6 | 20–24 | 1.0–1.2 | 33 |
| 3 | $8^h59^m04\overset{s}{.}70$ | −47°29′58″.3 | 0.015/3090 | 0.8 | 3.3–4.1 | 13–15 | 1.4–1.6 | 11 |
| 4 | $8^h59^m08\overset{s}{.}35$ | −47°30′12″.0 | 0.006/1340 | 0.8 | 2.6–3.2 | 2–2 | 3.0–3.3 | 4 |
| 5 | $8^h59^m01\overset{s}{.}42$ | −47°30′12″.0 | 0.014/2980 | 1.0 | 1.1–1.3 | 4–6 | 0.6–0.7 | 16 |
| 6 | $8^h59^m02\overset{s}{.}33$ | −47°30′19″.5 | 0.019/3990 | 1.6 | 2.6–3.1 | 23–27 | 1.1–1.3 | 60 |
| 7 | $8^h59^m03\overset{s}{.}19$ | −47°30′23″.0 | 0.020/4210 | 1.1 | 3.5–3.5 | 27–31 | 1.1–1.3 | 30 |
| 8 | $8^h59^m01\overset{s}{.}34$ | −47°30′29″.7 | 0.017/3440 | 0.9 | 2.8–3.4 | 17–20 | 1.3–1.5 | 17 |
| 9 | $8^h59^m01\overset{s}{.}54$ | −47°30′38″.0 | 0.024/4880 | 1.0 | 4.2–5.2 | 46–52 | 1.2–1.4 | 30 |
| 10 | $8^h59^m02\overset{s}{.}58$ | −47°30′41″.5 | 0.016/3280 | 1.3 | 3.8–4.2 | 17–19 | 1.5–1.7 | 30 |
| 11 | $8^h58^m59\overset{s}{.}86$ | −47°30′41″.7 | 0.019/4000 | 1.3 | 2.5–3.2 | 19–22 | 0.9–1.1 | 36 |
| 12 | $8^h59^m02\overset{s}{.}90$ | −47°30′44″.2 | 0.014/2780 | 1.0 | 4.4–6.7 | 18–18 | 2.6–2.6 | 14 |
| 13 | $8^h59^m03\overset{s}{.}69$ | −47°30′44″.8 | 0.015/3160 | 1.6 | 10.2–10.4 | 27–34 | 2.6–3.4 | 44 |
| 14 | $8^h59^m02\overset{s}{.}48$ | −47°30′47″.7 | 0.012/2410 | 0.7 | 2.8–3.6 | 8–8 | 1.8–2.0 | 6 |
| 15 | $8^h59^m00\overset{s}{.}55$ | −47°30′53″.2 | 0.018/3790 | 1.2 | 3.7–4.6 | 23–27 | 1.3–1.5 | 30 |
| 16 | $8^h58^m59\overset{s}{.}96$ | −47°30′57″.0 | 0.013/2750 | 1.4 | 4.4–4.4 | 14–16 | 2.2–2.5 | 29 |
| 17 | $8^h59^m01\overset{s}{.}29$ | −47°30′57″.2 | 0.012/2550 | 0.8 | 2.5–3.1 | 9–10 | 1.8–1.9 | 8 |
| 18 | $8^h59^m00\overset{s}{.}08$ | −47°31′00″.0 | 0.011/2250 | 1.3 | 5.2–8.2 | 10–15 | 2.7–4.1 | 21 |
| 19 | $8^h59^m00\overset{s}{.}63$ | −47°31′00″.7 | 0.011/2260 | 0.9 | 4.0–4.5 | 9–11 | 2.6–3.0 | 11 |
| 20 | $8^h59^m01\overset{s}{.}12$ | −47°31′02″.5 | 0.010/2120 | 0.8 | 3.4–5.9 | 7–10 | 2.5–3.5 | 7 |
| 21 | $8^h59^m00\overset{s}{.}41$ | −47°31′06″.0 | 0.010/2070 | 1.4 | 3.3–7.7 | 6–11 | 2.1–4.1 | 22 |

*$\sigma_v$ is the standard deviation of the velocity.
†$n_{H_2}$ was calculated from $M_{H_2}$ assuming a sphere with a radius of $r$.

The condensations have typical radius $r_{C^{18}O}$ of 0.01–0.02 pc (which correspond to ∼2000–4000 au) and are separated by 0.05–0.3 pc from each other. The $H_2$ column density $N_{H_2}$ and $H_2$ mass $M_{H_2}$ of the condensations were estimated assuming local thermodynamic equilibrium (LTE). These condensations show brightness temperatures $T_b$ of 30–50 K in the $^{13}CO_{all}$ data, and these values were used for the excitation temperature $T_{ex}$ in the calculations. A $[^{16}O]/[^{18}O]$ ratio of 550 and a $[H_2]/[^{12}CO]$ ratio of $10^4$ was adopted (e.g., Frerking et al. 1982; Leung et al. 1984; Wilson & Rood 1994). The derived $N_{H_2}$ are as high as an order of $10^{23}$–$10^{24}$ cm$^{-2}$ at the peak positions of the condensations, whereas the $M_{H_2}$ ranges from ∼10 to ∼100 $M_\odot$. We derived the virial mass, $M_{vir} = 210 r_{C^{18}O}(2\sqrt{2\ln 2}\sigma_v)^2$, assuming a uniform density inside the cores (MacLaren et al. 1988) without effects of the magnetic field and external pressure. The virial parameter, $\alpha_{vir} = M_{vir}/M_{H_2}$, is of the order of unity, suggesting that these condensations are gravitationally bounded. There are several $C^{18}O$ condensations with remarkably high $N_{H_2}$ of $10^{24}$ cm$^{-2}$, i.e., #1, #9, #10, #12, #13, #16, #18, and #19. The most dense and massive condensation #13 is located immediately west of IRS 1.

Figure 1c shows the ionized gas distribution in the H30$\alpha_{ACA}$ image. It shows a ring-like distribution, surrounding IRS 2, and is peaked at IRS 1. Figure 1d shows a magnified view of the $C^{18}O_{all}$ and H30$\alpha_{ACA}$ maps toward the condensation #13 and IRS 1, superimposed on the Very Large Telescope (VLT) near-infrared image (Wolk et al. 2006), indicating that the eastern rim of the condensation #13 follows the western rim of the bright ridge of IRS 1, and IRS 1 is spatially coincident with the H30$\alpha_{ACA}$ distribution. This result suggests that the bright infrared emission of IRS 2 arises from the strong irradiation of the outer envelope of the condensation by the adjacent IRS 2.

### 3.2 Discovery of two compact mm-sources: Source A and Source B

Figures 2a and 2b show millimeter/submillimeter continuum emission of 233 GHz$_{ACA}$ and 341 GHz$_{ACA}$, respectively. Two bright sources are detected in these two images. Hereafter, the two sources are referred to "Source A" and "Source B." Although the 341 GHz$_{ACA}$ image presents several clumpy structures without extended emission, the 233 GHz$_{ACA}$ image shows a ring-like extended emission, which resembles the recombination line emission in figure 1c. It is suggested that both the emission from cool dust grains and ionized gas are observed in the 233 GHz$_{ACA}$ image. Figure 2c shows distributions of the cool dust emission in the 233 GHz image with the highest spatial

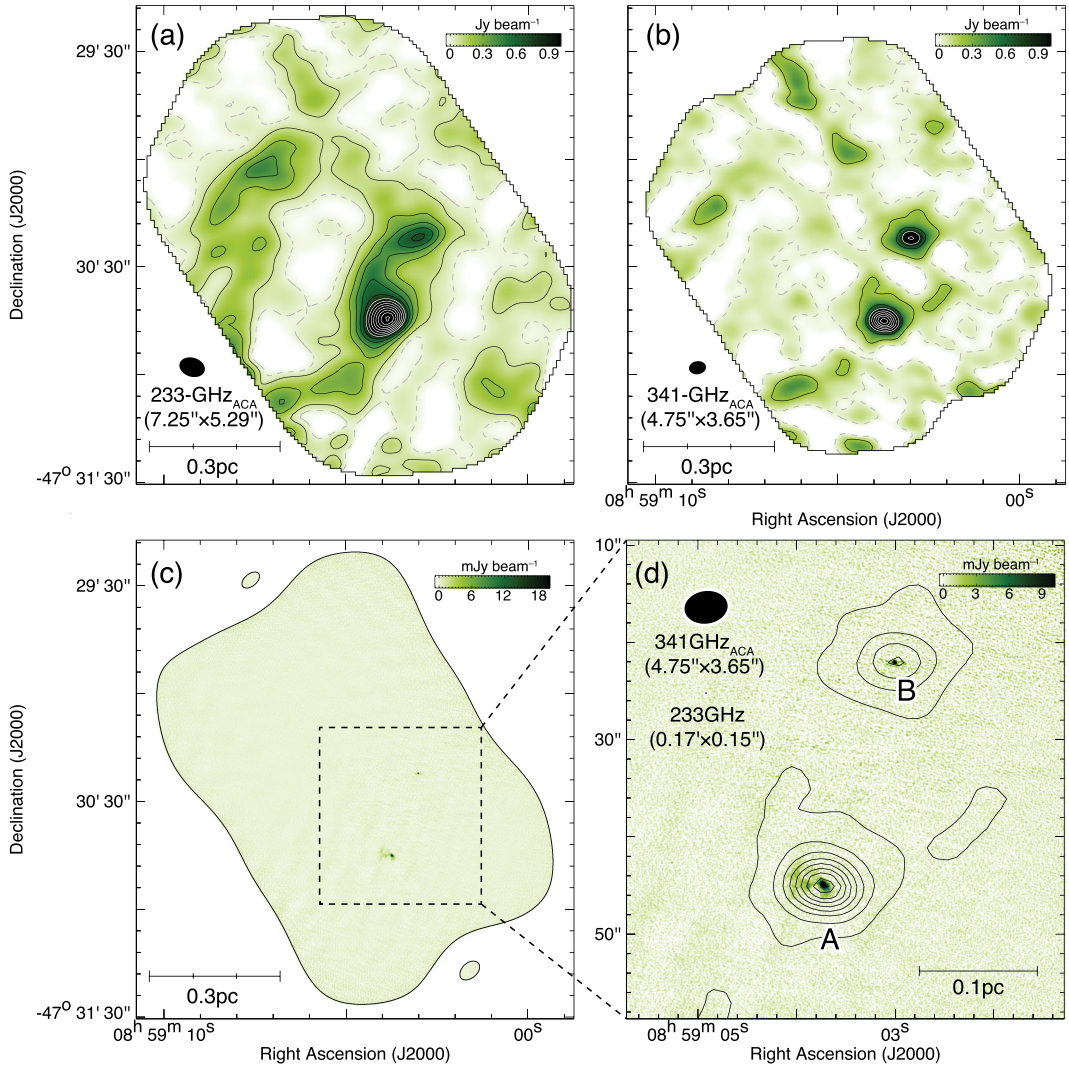


**Fig. 2.** (a) 233 $GHz_{ACA}$ image in the same region in figure 1, with contours starting at $5\sigma$ (0.19 Jy beam$^{-1}$) with steps of $10\sigma$ (0.37 Jy beam$^{-1}$). (b) 345 $GHz_{ACA}$ image, with contours starting at $5\sigma$ (0.07 Jy beam$^{-1}$) with steps of $10\sigma$ (0.15 Jy beam$^{-1}$). Contours with dashed lines are plotted at the zero level. (c) 233 GHz image. (d) Enlarged image of the 233 GHz data toward the box in panel (c). Contours show the 341 $GHz_{ACA}$ distribution, plotted at the same levels in panel (b).

resolution in this study. The two sources Source A and Source B are significantly detected, without any significant detections (above $3\sigma$) of other $C^{18}O$ condensations in this region, indicating that there are no compact/developed structures, such as protostellar disks, inside them. Figure 2d presents a magnified view of the 233 GHz image toward the corresponding region of figure 1d, with a contour map of 341 $GHz_{ACA}$.

Source A coincides with the condensation #13 west of IRS 1, whereas Source B is located 0.1–0.2 pc northwest of IRS 1 without any counterparts in the $C^{18}O$ condensations (figure 1c). As Source B is observed in the ACA map (figure 1c), which covers extended emission, the possibility of resolved-out can be dismissed to interpret the absence of $C^{18}O$ condensation.

Figure 3 shows an enlarged-view of Source A and Source B in the 233 GHz map with a resolution of $\sim 0\farcs16$. Both sources exhibit a single peak component. Source A shows a parallelogram-like distribution with a peak flux density of 24.9 mJy beam$^{-1}$, whereas Source B with a peak flux density of 48.8 mJy beam$^{-1}$ has a circular distribution, which is not fully resolved at the present spatial resolution. The obtained peak brightness temperatures of Source A and Source B correspond to $T_b$ values of 22 and 42 K, respectively. The relatively weak, diffuse emission located east of Source A, as shown in figure 3a, coincides with the western rim of IRS 1, which may be due to free–free emission, rather than thermal dust emission. We performed the aperture photometry toward both sources at the central $12''$ diameter in the 233 GHz map. The total fluxes of Source A and

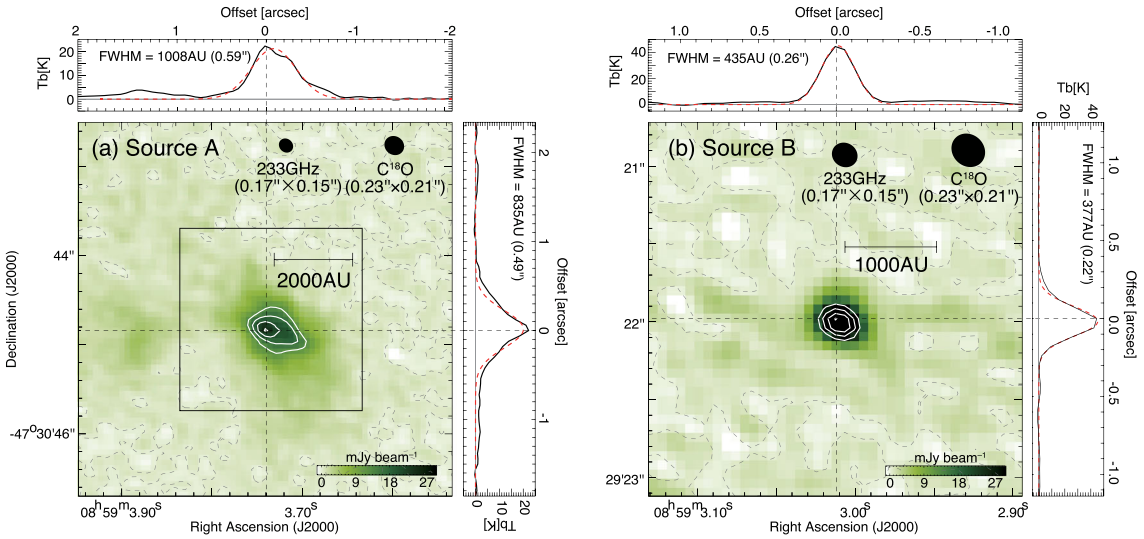


**Fig. 3.** Magnified views of the 233 GHz image for (a) Source A and (b) Source B. The white contours in panels (a) and (b) start at half of the peak intensities, 24.9 and 48.8 mJy beam$^{-1}$, with steps of 4 and 8 mJy beam$^{-1}$, respectively. The dashed contours are plotted at the zero level. Intensity profiles along the dashed lines across the peaks of the 233 GHz emission are plotted in black lines at the upper and right-hand sides of the panels in units of $T_b$, with the best-fitting Gaussian curves overlaid in dashed red lines.

Source B are 0.73 and 0.17 Jy, respectively. These figures account for approximately 24% and 13% of the total fluxes measured with the 233 GHz$_{ACA}$ map for the same areas. This result indicates that the 233 GHz data obtained with the 12 m array overlooks a significant amount of flux from the extended dust emission toward Source A and Source B.

The VLT/ISACC and NACO $J$, $H$, and $K_s$ images obtained by Wolk et al. (2006) and DeRose et al. (2009) indicate no significant excess of emission toward Source A or Source B. This is also the case for the four Spitzer/IRAC bands (3.4, 4.5, 5.6, and 8.0 $\mu$m; Wolk et al. 2006). Unfortunately, there are no available data with high angular resolution at infrared wavelengths exceeding 8 $\mu$m. Because of the non-detection of the available infrared observations, the two protostellar sources driving the molecular outflows are deeply embedded in the parental dense cores. This nature is consistent with the non-detection of H30$\alpha$ emission from the continuum peaks with the 12 m array, meaning that the young sources do not start to ionize their surroundings.

## 3.3 Physical properties of Source A and Source B

Tables 4 and 5 summarize the physical parameters of Source A and Source B estimated from the 233 GHz and 341 GHz$_{ACA}$ maps.

### 3.3.1 341 GHz$_{ACA}$ data

The 233 GHz$_{ACA}$ image recovers extended structures (figure 2a), but the ring-like morphology is quite similar to the H30$\alpha$ distribution (figure 1c). This means that the ionized gas (i.e., free–free) emission contaminates the 233 GHz$_{ACA}$ image (see subsection 3.2). We thus used the 341 GHz$_{ACA}$ map (figures 2b and 2d), the distribution of which reasonably agrees with that in C$^{18}$O (figure 1a) tracing cold/dense materials, to estimate the core properties of Source A and Source B. The physical parameters measured from the 341 GHz$_{ACA}$ map, which has an angular resolution of $\sim$4″, are as follows; the radii of Source A and Source B at the half maxima, $r_{dust}$, are as small as $\sim$0.02 and $\sim$0.03 pc, respectively.

The $N_{H_2}$ and $M_{H_2}$ of the sources were calculated from the peak and total fluxes of the sources ($S_{peak}$ and $S_{int}$) at the optically thin limit as follows;

$$N_{H_2} = \frac{R_{g/d} S_{peak,\nu}}{2.8\, m_H \kappa_\nu B_\nu(T_{dust}) \Omega_{beam}}, \quad (1)$$

$$M_{H_2} = \frac{R_{g/d} S_{int,\nu} D^2}{\kappa_\nu B_\nu(T_{dust})}, \quad (2)$$

where $T_{dust}$ is the dust temperature and $R_{g/d}$ is the gas-to-dust ratio. Here, an $R_{g/d}$ of 100 was assumed. The dust opacity $\kappa_\nu$ at 341 GHz was assumed to be 1.8 cm$^{-2}$ g$^{-1}$ from a thin ice mantle model of Ossenkopf and Henning (1994) for a density of $10^6$ cm$^{-3}$. $B_\nu(T_d)$ is the Planck function for $T_d$. Far-infrared and submillimeter continuum observations indicate that cold dust components embedded within the H II regions typically have a $T_{dust}$ of 15–30 K (e.g., Anderson et al. 2012; Torii et al. 2017b; Motte et al. 2018). Considering the proximity of the exciting stars to

**Table 4.** Measured parameters of Source A and Source B.

| | | | 341 GHz$_{ACA}$ (4.″75 × 3.″65) | | 233 GHz (0.″17 × 0.″15) | |
|---|---|---|---|---|---|---|
| Source | RA (J2000.0) | Dec (J2000.0) | $S_{peak}$ (Jy beam$^{-1}$) | $S_{int}$* (Jy) | $S_{peak}$ (mJy beam$^{-1}$) | $S_{int}$* (Jy) |
| A | $8^h59^m3.^s740$ | −47°30′44.″832 | 3.1 | 4.9(0.6) | 24.9 | 0.24(0.07) |
| B | $8^h59^m3.^s013$ | −47°30′21.″982 | 1.4 | 2.5(0.8) | 48.8 | 0.11(0.05) |

*The aperture radii of the photometry for measuring $S_{int}$ were set to 6.″5 and 0.″5 for the 341 GHz$_{ACA}$ image and the 233 GHz image, respectively. In the 341 GHz$_{ACA}$ image, the local background level of each source was estimated around the source using a circular annulus with inner and outer radii of 6.″5 and 1.5 × 6.″5 = 9.″8, respectively. The median value of the pixels within the annulus was applied as the local background level, with the standard deviation applied as the uncertainty of the photometry. The derived uncertainty is shown in parentheses.

**Table 5.** Physical properties of Source A and Source B.

| | 341 GHz$_{ACA}$ (4.″75 × 3.″65) | | | 233 GHz (0.″17 × 0.″15) | | |
|---|---|---|---|---|---|---|
| Source | $r_{dust}$* (pc) | Peak $N_{H_2}$† (×10$^{23}$ cm$^{-2}$) | $M_{H_2}$† ($M_\odot$) | $r_{dust}$* (au) | Peak $N_{H_2}$† (×10$^{24}$ cm$^{-2}$) | $M_{H_2}$† ($M_\odot$) |
| A | 0.02 | 10.7–26.8 | 32(3.9)–81(9.9) | 460 | 6 | 5(3.8) |
| B | 0.03 | 4.9–12.2 | 16(5.1)–41(13.1) | 200 | 6 | 2(1.2) |

*$r_{dust}$ was measured at the half maximum.
†$N_{H_2}$ and $M_{H_2}$ were estimated at the optically thin limit. $T_d$ values of 20 and 40 K were assumed in the $N_{H_2}$ and $M_{H_2}$ estimated from the 341 GHz$_{ACA}$ image to constrain $M_{H_2}$ ranges of the sources, whereas in the 233 GHz image, 100 K (see the text) was used as $T_d$, for Source A and Source B, respectively (figure 3). The statistical uncertainty of the derived $M_{H_2}$ is shown in parentheses. Note that systematic errors arising from uncertainties of the distance measurement and the assumption of gas-to-dust ratio/opacity give a further uncertainty factor of ∼2.

Source A and Source B, which may lead to higher temperatures, $T_{dust}$ values of 20–40 K were assumed in this study. As a result, the $N_{H_2}$ values at the peaks of the two sources were calculated to be 1.1–2.7 × 10$^{24}$ cm$^{-2}$ for Source A and 0.5–1.2 × 10$^{24}$ cm$^{-2}$ for Source B, whereas the $M_{H_2}$ values were as large as 32–81 $M_\odot$ for Source A and 16–41 $M_\odot$ for Source B. The number densities of the condensations $n_{H_2}$ were calculated as an order of 10$^7$ cm$^{-3}$ from the $M_{H_2}$ assuming a sphere.

The 3$\sigma$ mass-detection limit of the 341 GHz$_{ACA}$ image is approximately 3–6 $M_\odot$, depending on the $T_d$ assumption (15–30 K). Although we detected some additional C$^{18}$O cores, such as #4 and #5, their masses are similar to or lower than the continuum detection limit.

### 3.3.2 233 GHz data

The physical parameters of Source A and Source B measured from the high-resolution 233 GHz data are as follows. The $r_{dust}$ values of Source A and Source B were measured by fitting the horizontal and vertical profiles across the peaks with a Gaussian function, with values of ∼460 and ∼200 au, respectively (figure 3). Because it is difficult to measure the optical depths of the sources with the present dataset, we assumed the optically thin case to estimate the $N_{H_2}$ and $M_{H_2}$ using equations (1) and (2) with a $\kappa_\nu$ of 0.899 cm$^{-2}$ g$^{-1}$, and an $R_{g/d}$ of 100. Since the observed peak $T_b$ values of 22 K for Source A and 42 K for Source B in the 233 GHz image are presumably the lower limit as the actual temperature, we adopted $T_d$ = 100 K based on the recent molecular line measurements toward the G353.273+0.641 high-mass protostellar disk (Motogi et al. 2019). The derived $N_{H_2}$ value is approximately 6 × 10$^{24}$ cm$^{-2}$ for the two sources, with the $M_{H_2}$ values calculated as ∼5 $M_\odot$ for Source A and ∼2 $M_\odot$ for Source B. Observations at lower frequencies are crucial for measuring $N_{H_2}$ and $M_{H_2}$ more accurately by quantifying the optical depth of the dust emission.

Note that we could not detect any other emission in the 233 GHz continuum image (see figure 2). Recent ALMA surveys with the 12 m array in the nearby low-mass star-forming regions demonstrated that it is hard to detect millimeter/submillimeter continuum emission in starless sources due to the lack of compact features, such as protostellar disks, inside them (Dunham et al. 2016; see also Tokuda et al. 2020). It is thus likely that the other cores in the observed RCW 38 field are intrinsically in the starless phase.

### 3.3.3 Velocity distribution of the C$^{18}$O emission in Source A

The high-resolution C$^{18}$O data were analyzed to investigate the molecular gas components associated with Source A. Figure 4a shows the intensity distribution of the C$^{18}$O data integrated over a velocity range of −2 to +4 km s$^{-1}$, in

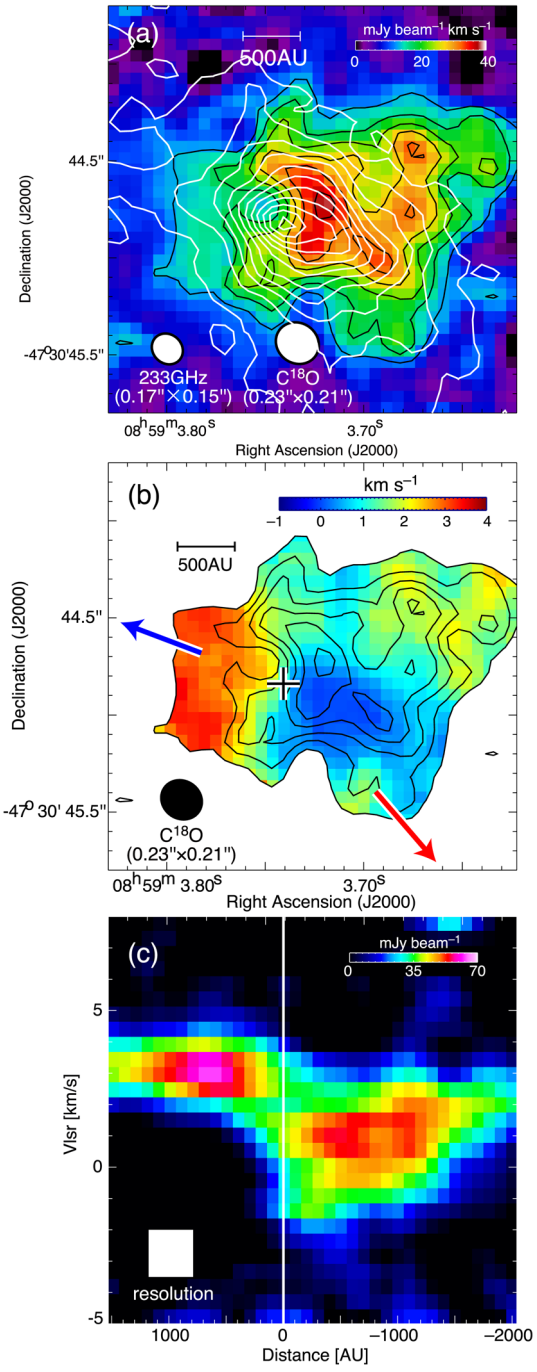


**Fig. 4.** (a) Intensity distribution of the $C^{18}O$ data (color and black contours) and the 233 GHz map (white contour) for Source A. The velocity integration range is −2 to +4 km s$^{-1}$. The black contours start at 3$\sigma$ (135 mJy beam$^{-1}$ km s$^{-1}$) with steps of 1$\sigma$ (45 mJy beam$^{-1}$ km s$^{-1}$), whereas the white contours start at 3$\sigma$ (1.35 mJy beam$^{-1}$) with steps of 5$\sigma$ (2.25 mJy beam$^{-1}$). (b) First moment map of the $C^{18}O$ data (color) superimposed with the contour map of the $C^{18}O$ data in panel (a). The cross indicates the peak position of the 233 GHz image. The two arrows indicate the directions of the blueshifted and redshifted outflow lobes shown in figure 6. (c) Position–velocity diagram of the $C^{18}O$ data. The $C^{18}O$ data were smoothed to be a velocity resolution of 1.5 km s$^{-1}$. The vertical white line indicates the direction of the 233 GHz peak of Source A.

which the $C^{18}O$ emission was detected in the presented region. The $C^{18}O$ distribution is more extended than the 233 GHz distribution, and the peak position does not perfectly coincide with the peak of the 233 GHz map, as shown by the white contours.

Figure 4b shows a first moment map of the $C^{18}O$ data. A clear velocity gradient along the southwest–northeast direction is present, which can also be observed in the position–velocity (p-v) diagram in figure 4c. The p-v diagram shows two velocity components, at ∼−1 and ∼3 km s$^{-1}$ and located west and east of the 233 GHz peak, respectively, and the 233 GHz peak is located in the center of the intermediate-velocity feature connecting the two velocity components. These observed signatures suggest rotational motion of the $C^{18}O$ component centered on the 233 GHz peak. However, the directions of the outflow lobes which will be presented in the next subsection are not perpendicular to the direction of the velocity gradient (see arrows in figure 4b). This is inconsistent with the hypothesis that the observed $C^{18}O$ component is a protostellar disk. Infall motion of gas, the velocity of which is proportional to $r^{-1}$ (e.g., Ohashi et al. 2014), is an alternative idea to explain the observed velocity gradient. It is difficult to distinguish these two possibilities with the sensitivity and velocity resolution of the observed p-v diagram. If the velocity gradient was purely attributed to the Keplerian rotation, as the $C^{18}O$ distribution does not perfectly match the 233 GHz distribution, the obtained result does not immediately indicate that Source A harbors a protostar with a mass of a few × $M_\odot$. Indeed, Zhang et al. (2019) highlighted the importance of the choice of molecular lines in investigating the rotational motion to directly determine the mass of the central object.

### 3.4 High-velocity molecular outflows for Source A and Source B

In this subsection we report the discovery of high-velocity molecular outflows associated with Source A and Source B. The physical properties of the outflow lobes are summarized in table 6. Figure 5 shows the spectra obtained from the $^{12}CO_{ACA}$ and $C^{18}O_{ACA}$ toward the 341 $GHz_{ACA}$ peaks of Source A and Source B (figure 1d). Wing features with velocity widths of ∼30–70 km s$^{-1}$ are clearly present in the $^{12}CO$ spectra for both the blueshifted and redshifted velocity ranges of Source A and Source B.

Figure 6a shows the spatial distributions of the outflow lobes in Source A from the high-resolution $^{12}CO$ data, whereas figure 6b presents velocity distributions of the outflow lobes, defined as $|v_{mom1} - v_{sys}|$, where $v_{mom1}$ and $v_{sys}$ are the first moment and systemic velocity of the source,

**Table 6.** Physical properties of the outflow lobes.*

| Lobes | $v_{max}/\sin i$ (km s$^{-1}$) | $l_{max}/\cos i$ (au) | $t_{dyn}/\tan i$ (yr) | $M_{lobe}$ ($M_\odot$) | $\dot{M}_{lobe}/\tan i$ ($M_\odot$ yr$^{-1}$) |
|---|---|---|---|---|---|
| (Source A: $v_{sys} = 2$ km s$^{-1}$) | | | | | |
| Blueshifted lobe | 24 | 3200 | 630 | 0.06 | $0.10 \times 10^{-3}$ |
| Redshifted lobe | 38 | 9100 | 1100 | 0.4 | $0.36 \times 10^{-3}$ |
| (Source B: $v_{sys} = 5$ km s$^{-1}$) | | | | | |
| Blueshifted lobe | 67 | 10600 | 750 | 1.3 | $1.7 \times 10^{-3}$ |
| Redshifted lobe | 45 | ... | ... | 0.3 | ... |

*$v_{max}$ is the maximum velocity of the outflow lobe measured from the systemic velocity $v_{sys}$ of the source, whereas $l_{max}$ is the physical length of the lobes measured from the 233 GHz peak of the source. The dynamical timescale of the outflow $t_{dyn}$ was calculated as $t_{dyn} = l_{max}/v_{max}$. The $H_2$ mass of the outflow lobe was calculated using a CO-to-$H_2$ conversion factor of $2 \times 10^{20}$ (K km s$^{-1}$)$^{-1}$ cm$^{-2}$ (Bolatto et al. 2013). The mass flow rate $\dot{M}_{lobe}$ was measured as $M_{flow}/t_{dyn}$. The $l_{max}$ of the redshifted lobe in Source B could not be measured.

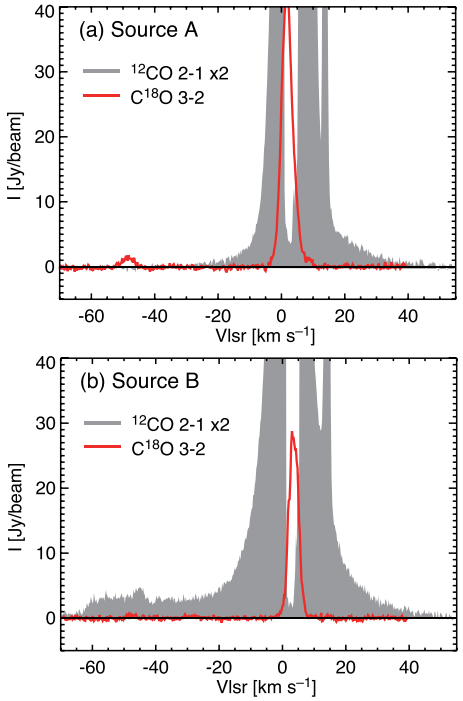


**Fig. 5.** Spectra of the $^{12}CO_{ACA}$ and $C^{18}O_{ACA}$ data near the peaks of the 233 GHz map for Source A and Source B. The intensities of the $^{12}CO_{ACA}$ are doubled.

respectively. The $v_{sys}$ value was determined from the $C^{18}O_{ACA}$ spectra in figure 5 as 2 km s$^{-1}$.

As shown in figure 6a, the blueshifted and redshifted lobes are elongated from Source A toward the northeast–southwest direction by ~3200 and ~9100 au, respectively. These two lobes are not perfectly aligned with each other, and the outflow axis does not correspond to the rotational axis of the $C^{18}O$ component (see arrows in figure 4b). In the blueshifted velocity range, other weak emission is observed north and south of the lobe, but it is difficult to determine whether these features are associated with Source A, as the signal-to-noise ($S/N$) ratio of the present ALMA molecular line data is not high. The triangle in figure 6a depicts the position of the $H_2$ emission at 2.12 $\mu$m reported by DeRose et al. (2009) using VLT/NACO, which is located near the tip of the blueshifted lobe, suggesting the presence of shocked molecular gas caused by the outflow.

As shown in figure 6b, the redshifted lobe has a velocity gradient along the lobe, whereas such a gradient is not clear in the blueshifted lobe. Given the maximum velocities $v_{max}$ of 27 and 38 km s$^{-1}$, the dynamical timescales of the blueshifted and redshifted lobes $t_{dyn}$ were estimated as 560 and 1100 yr, respectively, depending on their inclination angles, $i$, which is defined as 0° for the plane of the sky. It is not simple to measure the $H_2$ masses of the outflow lobe $M_{lobe}$, because this value strongly depends on the line opacity, excitation temperature, inclination, and so on; moreover, it is difficult to distinguish the effects of these parameters for the relatively low-$S/N$ ratio of the line data obtained with the 12 m array. However, using the synthetic observation technique, Offner et al. (2011) demonstrated that the CO-to-$H_2$ conversion factor can be used to track the actual mass of the outflow over different epochs, although the derived $M_{lobe}$ is generally a factor of 5–10 smaller than the actual mass due to the opacity effect. Therefore, in this study we adopt a CO-to-$H_2$ conversion factor of $2 \times 10^{20}$ (K km s$^{-1}$)$^{-1}$ cm$^{-2}$ (Bolatto et al. 2013), as a conservative way to estimate the lower-limit of $M_{lobe}$. The derived $M_{lobe}$ values of the blueshifted and redshifted lobes were 0.06 and 0.4 $M_\odot$, respectively (table 6). If we assume the inclination angle of 30°–70°, the mass outflow rates $\dot{M}_{lobe}$ of the two lobes were derived as (0.4–1.6) $\times$ $10^{-4}$ and (1.3–6.3) $\times$ $10^{-4}$ $M_\odot$ yr$^{-1}$, respectively.

Compared with the lobes in Source A, the blueshifted lobe in Source B is relatively expanded, showing a cocoon-like shape. The $v_{max}$ of the blushifted lobe is found to be as high as 67 km s$^{-1}$, and the velocity increases within the cocoon (figure 7b). In contrast, the redshifted lobe does not show a clear shape; rather a weak, diffuse component is observed toward Source A. Although two other weak features are observed northwest of Source B in the redshifted

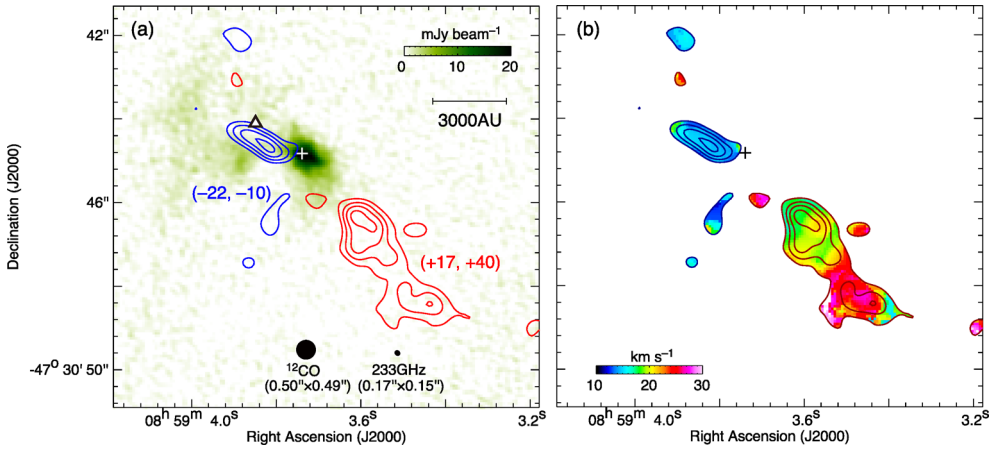


**Fig. 6.** (a) $^{12}$CO intensity distributions of the blueshifted and redshifted outflow lobes shown in blue and red contours, respectively, with the 233 GHz background image. The velocity ranges of the lobes are shown in parentheses in units of km s$^{-1}$. The contours stars at 3 $\sigma$ with steps of 1.5 $\sigma$, where the 1 $\sigma$ value of the blueshifted and redshifted maps of Source A are 30 and 65 mJy beam$^{-1}$ km s$^{-1}$, respectively. The triangle depicts the approximate position of the vibrational transition of the $H_2$ emission detected by VLT (DeRose et al. 2009). (b) Color map of $|v_{\rm mom1} - v_{\rm sys}|$ for the lobes, with the $^{12}$CO contour maps plotted in panel (a), where $v_{\rm mom1}$ is the first moment generated from the $^{12}$CO data for the velocity ranges shown in panel (a), whereas the systemic velocity of the source $v_{\rm sys}$ was measured from the C$^{18}$O$_{\rm ACA}$ data as 2 km s$^{-1}$ (figure 5). The cross indicates the 233 GHz peak for Source A.

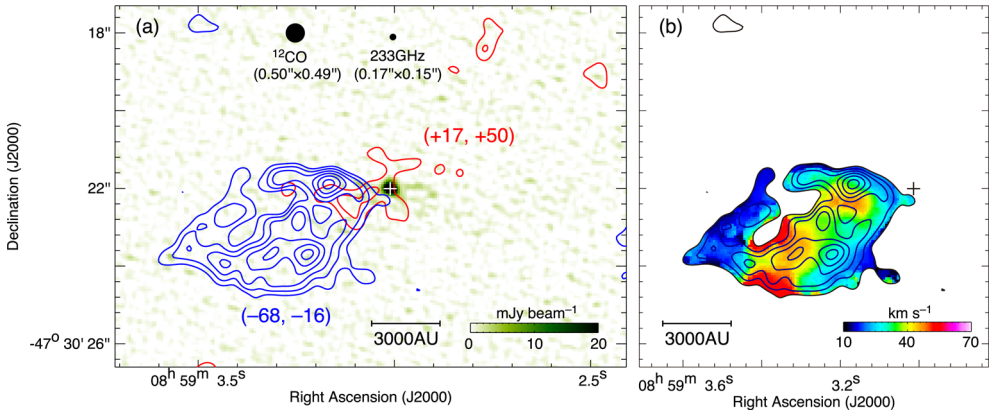


**Fig. 7.** The same plots shown in figure 6 are presented here, but for Source B. In panel (a), the 1 $\sigma$ levels of the $^{12}$CO maps are 90 and 100 mJy beam$^{-1}$ km s$^{-1}$ for the blueshifted and redshifted lobes, respectively. In panel (b), only the blueshifted lobe is plotted.

velocity range, the association of these features with the redshifted lobe cannot be confirmed at this time. The projected length of the blueshifted lobe is ~10000 au, providing a short $t_{\rm dyn}$ of 750 yr (table 6). The possible range of the mass-loss rate is (0.7–3) × $10^{-3}$ $M_\odot$ yr$^{-1}$ with the same assumption of $i$ in the previous paragraph.

## 4 Discussion

### 4.1 Source A and Source B; nurseries of massive protostars?

The present ALMA data revealed two compact mm-sources at the center of the young super star cluster RCW 38. The two sources are embedded within dust condensations with $r_{\rm dust}$ of ~0.02–0.03 pc and $M_{\rm H_2}$ greater than ~20–30 $M_\odot$ (table 5). These condensations seem to satisfy the initial conditions for the massive star formation (e.g., Tan et al. 2014), at least in their mass-concentrated nature. The mechanical force of the outflows, $F_{\rm out} = M_{\rm lobe} v_{\rm max}/t_{\rm dyn}$, is the order of $10^{-2}$ $M_\odot$ km s$^{-1}$ yr$^{-1}$, which is consistent with that of known high-mass protostars compiled by Maud et al. (2015). Since the mass accretion rate $\dot{M}_{\rm acc}$ correlates with the outflow mass rate ($\dot{M}_{\rm acc} \simeq$ a few × $\dot{M}_{\rm lobe}$) (Beuther et al. 2002; Maud et al. 2015), the observed high $\dot{M}_{\rm lobe}$ values suggest a high $\dot{M}_{\rm acc}$ of the order of $10^{-4}$–$10^{-3}$ $M_\odot$ yr$^{-1}$ for Source A and Source B, which is consistent with the values obtained with massive star formation models (e.g., McKee & Tan 2003; Hosokawa & Omukai 2009; Hosokawa et al. 2010). These observational signatures imply that Source A and Source B harbor massive protostars that can drive energetic outflows. Note that the two sources exhibit a single

peak at the 270au resolution, indicating no signs of fragmentation.

Further, the short $t_{\rm dyn}$ values of the outflow lobes in Source A and Source B suggest that these protostars are in an early evolutionary stage. If $t_{\rm dyn}$ is interpreted as the age of the protostar driving the outflow, it should coincide with the accretion time $t_{\rm acc}$, suggesting that the total $M_{\rm lobe}$ of the outflow lobes, $\sim 0.5\,M_\odot$ for Source A and $\sim 1.6\,M_\odot$ for Source B.

### 4.2 Infrared-quiet sources

Measuring the luminosity at infrared wavelengths is another way to constrain the evolutionary stage of the protostars. However, infrared images above 8.0 $\mu$m are not available in RCW 38 at an angular resolution of a few arcseconds. Further, no significant emission was detected for Source A and Source B in the near- and mid-infrared wavelengths below 8.0 $\mu$m; the VLT and Spitzer/IRAC images do not show any excess toward these two sources. If we adopt an accretion rate of $10^{-4}$–$10^{-3}\,M_\odot\,{\rm yr}^{-1}$ (subsection 4.1) on to the central protostars inside Source A/B, equation (22) in Hosokawa and Omukai (2009) tells us that the temperature of the accretion gas is 100–500 K. In this case, the peak of the spectral energy distribution should be in near- or mid-infrared wavelengths. Here, the Spitzer/IRAC 3.6, 4.5, 5.6, and 8.0$\mu$m archival images (Wolk et al. 2006) were used to estimate the upper limit of the luminosity at 3.6–8.0 $\mu$m ($L_{3.6-8.0}$) for Source A and Source B, by integrating the upper limits of the flux in the four bands. The upper limit of the flux in each band was measured as the standard deviation of the flux density distribution around a 4″ area of the source, and the derived upper limits range $\sim$100–400 MJy str$^{-1}$ for the four bands. The $L_{3.6-8.0}$ values, which are not the bolometric luminosity, were then calculated to be as small as $3.0\,L_\odot$ for Source A and $1.6\,L_\odot$ for Source B. Inclusion of the $J$, $H$, and $K_{\rm s}$ bands does not strongly change these values.

In these wavelengths, accreting gas as well as the protostar itself should be the major sources of the emission. The accretion luminosity $L_{\rm acc}$ can be calculated as follows:

$$L_{\rm acc} = \frac{GM_*\dot{M}_{\rm acc}}{R_*} \simeq 1219\left(\frac{M_*}{1\,M_\odot}\right)\left(\frac{\dot{M}_{\rm acc}}{10^{-3}\,M_\odot\,{\rm yr}^{-1}}\right) \times \left(\frac{26\,R_\odot}{R_*}\right)\,[L_\odot], \quad (3)$$

where $G$ is the gravitational constant, and $M_*$ is the stellar mass. The stellar radius $R_*$ can be given as a function of $M_*$ and $\dot{M}_{\rm acc}$ (Stahler et al. 1986; Hosokawa & Omukai 2009):

$$R_* \simeq 26\left(\frac{M_*}{1\,M_\odot}\right)^{0.27}\left(\frac{\dot{M}_{\rm acc}}{10^{-3}\,M_\odot\,{\rm yr}^{-1}}\right)^{0.41}\,[R_\odot]. \quad (4)$$

Assuming that $\dot{M}_{\rm acc}$ is equal to the total $\dot{M}_{\rm lobe}$ of the redshifted and blueshifted lobes, the expected $L_{\rm acc}$ for $M_*$ of 0.1 and 1 $M_\odot$ is calculated as 140 and 770 $L_\odot$ for Source A and 310 and 1700 $L_\odot$ for Source B, respectively. Even for a small $M_*$ of 0.1 $M_\odot$, the derived $L_{\rm acc}$ is approximately two orders of magnitude larger than the derived upper limits of $L_{3.6-8.0}$ for Source A and Source B.

A reasonable interpretation of the low $L_{3.6-8.0}$ is that the dusty envelopes of Source A and Source B veil the luminous accreting gas in near- and mid-infrared wavelengths. The two dust condensations have $N_{\rm H_2}$ of higher than $10^{24}$ cm$^{-2}$ (see figure 1d and table 5). If the dust opacity model from Ossenkopf and Henning (1994) is assumed, the optical depths of the dust emission at 3.6–8.0 $\mu$m can be calculated to be $\sim$50–100 at $N_{\rm H_2} = 10^{24}$ cm$^{-2}$. The emission of the accreting gas cannot be observed at these high optical depths. However, the opacity effect strongly depends on the three-dimensional inner structures of the sources. If there is a hole created by the outflows in the condensation and if the inclination of the hole is not perpendicular to us, the emission from the accreting gas could be detected through the hole (e.g., Motogi et al. 2017, 2019).

Another idea is "episodic accretion." This idea was originally studied in low-mass star formation, followed by recent studies on the massive star formation models (e.g., Hosokawa et al. 2016; Meyer et al. 2017, 2018). In the episodic accretion scenario, protostars spend most of their time in the quiescent phase with a low $\dot{M}_{\rm acc}$, interspersed with short but intense accretion bursts caused by disc gravitational fragmentation followed by rapid migration of the fragments on to the protostar (e.g., Dunham & Vorobyov 2012; Hosokawa et al. 2016). Therefore, the quiescent phase with a low $L_{\rm acc}(\propto \dot{M}_{\rm acc})$ has a high probability of detection, whereas the $\dot{M}_{\rm lobe}$ of the outflows may be high, as it is calculated as a time-averaged value.

Further investigation of these scenarios for Source A and Source B should be performed based on high-resolution observations. Observations at lower frequencies, where dust opacity is less influential, for instance, for ALMA band 3, are important for accurately measuring the source masses. A high angular resolution, increased by a factor of two or three, is crucial to obtain detailed mass distributions of the sources. Observations with various molecular lines are also important for investigating the rotational motion of Source A and Source B. If Keplerian motion can be confirmed, the mass of the protostellar object can be measured.

Molecular line observations are also important to investigate the possibility of CO depletion in Source B.

### 4.3 Formation of massive condensations in RCW 38

Source A and Source B are found inside molecular condensations embedded within the filamentary structures, with a width of ∼0.1–0.2 pc, extending along the northeast–southwest direction in RCW 38 (figure 1). The filamentary structures include 21 $C^{18}O$ condensations with large $N_{H_2}$ values of $>10^{23}$ cm$^{-2}$ and $M_{H_2}$ values of $>10\,M_\odot$ (table 3). Although no 233 GHz continuum sources were detected in any of the condensations except for #13, which harbors Source A, there are no such massive/dense starless objects in nearby low-mass star-forming regions (e.g., Onishi et al. 2002; Tachihara et al. 2002). The observed core properties, especially mass and size, in RCW 38 are consistent with those in infrared dark clouds on the Galactic plane (e.g., Ohashi et al. 2016), indicating that the identified condensations are likely precursors of high-mass or at least intermediate-mass stars. Recent numerical simulations successfully demonstrated that a massive/compact dense core, the mass and size of which are $100\,M_\odot$ and 0.1 pc, respectively, monolithically collapses into high-mass stars in a similar manner to low-mass star formation, which is referred to as the turbulent core accretion scenario (e.g., McKee & Tan 2003; Krumholz et al. 2009). Krumholz, Klein, and McKee (2012) simulated the evolution of a larger system with a gas mass of $\sim1000\,M_\odot$ and ∼0.4 pc, and pointed out that supersonic gas flows within the parental cloud produce filamentary structures with a few overdense spots, each of which looks like the turbulent core posted by McKee and Tan (2003). One of the crucial questions is what mechanism drives the creation of such a massive (100–$1000\,M_\odot$) and compact gas clump with a sub-parsec size scale, adopted as the initial condition of the cloud-collapse simulations, without a significant mass consumption due to lower-mass star formation (for a review see Fukui et al. 2021a).

The formation of the filamentary structures and massive condensations may be attributed to strong compression caused by feedback from adjacent O stars through a process known as "collect and collapse" (Elmegreen & Lada 1977). In this model, an expanding HII region sweeps the surrounding medium, forming a dense molecular shell, which is followed by the fragmentation and formation of new stars. In the case of RCW 38, however, the distance between the massive condensations and exciting source (IRS 2) is too small for the accumulated gas to induce fragmentation. The lengths of semi-major and minor axis of the ring-like structure in H30$\alpha$ are ∼0.3 and ∼0.2 pc, respectively (see figure 1c). If we assume that a spherical geometry of the ionized gas and the location of IRS 2 is the center, the distance between the central source and Source A/B is at most ∼0.3 pc even when we consider the projection effect. Because the small distance is roughly the same as the width of the filamentary structures, the gas density $n_{H_2}$ in the accumulated layer can increase by a factor of only ∼2 from the initial gas density, if a plane-parallel is assumed; however, the model calculation requires that $n_{H_2}$ be increased by one or two orders of magnitude (e.g., Hosokawa & Inutsuka 2006). Thus, it is more likely that the seeds of the massive condensations holding Source A and Source B were formed prior to the onset of ionization of the O stars, although it is still possible that the feedback from nearby O stars enhanced the accretion of the condensations (e.g., Shima et al. 2017).

On the other hand, as summarized in the Introduction, it is suggested that the formation of massive stars in RCW 38 was triggered by a collision between two molecular clouds with a velocity separation of ∼10 km s$^{-1}$ (Fukui et al. 2016). Recent ALMA observations of giant molecular clouds in the Large Magellanic Cloud found hub-filamentary structures (Myers 2009), in which massive stars are being formed, and these structures were likely formed by a large-scale colliding flow (Fukui et al. 2019; Tokuda et al. 2019a; see also André et al. 2016 for the case of NGC 6334 in the Milky Way). Numerical calculations indicate that such a supersonic collision would create a network of filaments with widths of a few 0.1 pc at the interface of the collision (Inoue & Fukui 2013; Inoue et al. 2018). Fukui et al. (2020b) analyzed the data of the numerical simulations of cloud–cloud collision in Inoue and Fukui (2013), finding that the massive cores are efficiently formed within the filaments created through the cloud–cloud collision. These massive cores are separated with each others by ∼0.05–0.2 pc, which are consistent with the separations of the observed condensations in RCW 38 (figure 1a). Although the thermal Jeans instability with a volume density of $10^4$–$10^5$ cm$^{-3}$ may also describe the core separation, the observed density and mass are one or two orders of magnitude higher than those in the fragmentation mode. The observed massive/dense nature of the condensations along the filament in RCW 38 could be indirect evidence that they may be products of an intense gas compression event, such as cloud–cloud collision. Once such a compression makes gravitationally unstable massive cores, they eventually collapse into high-mass protostars following the core accretion scenario (e.g., Tan et al. 2014).

The competitive accretion (e.g., Bonnell et al. 2001) may alternatively realize the mass accretion rate of $\sim10^{-4}\,M_\odot$ yr$^{-1}$ (Wang et al. 2010), and thus we cannot fully exclude the competitive accretion scenario for

high-mass star formation in the RCW 38 region. Ascenso (2018) summarized that cloud–cloud collisions are one of the promising origins as a trigger of the formation of an isolated O-star system, such as M 20 and RCW 120 (Torii et al. 2011, 2015), while the competitive accretion scenario may not be applicable to such a compact system of small mass (Fukui et al. 2021a). Cloud–cloud collisions are a versatile mechanism which explains the high-mass star (cluster) formation throughout various interstellar scales. To quantitatively investigate whether or not the competitive accretion can be applied in RCW 38, we need a further detailed comparison between the observations and numerical models, which is beyond the scope of the present study.

## 5 Summary

The conclusions of the present study are summarized as follows.

(1) The molecular gas associated with the Galactic super star cluster RCW 38 is resolved at the 270 au scale using the new ALMA cycle-3 band-6 and band-7 data. The $C^{18}O$ image was used to identify the filamentary structures with a width of 0.1–0.2 pc, which contains 21 condensations with $r_{C^{18}O}$ of 0.01–0.02 pc, peak $N_{H_2}$ of $10^{23}$–$10^{24}$ cm$^{-2}$, and $M_{H_2}$ of 10–130 $M_\odot$.

(2) In addition, the high-resolution 233 GHz continuum data revealed two dense, compact mm-sources (Source A and Source B) with radii of ∼460 and ∼200 au. The $N_{H_2}$ of the two sources was derived as an order of $10^{24}$ cm$^{-2}$, whereas the $M_{H_2}$ were estimated as 13 $M_\odot$ for Source A and 3 $M_\odot$ for Source B at the optically thin limit. Source A is coincident with one of the $C^{18}O$ condensations, whereas no counterpart is found for Source B. The $C^{18}O$ condensation holding Source A is located immediately west of IRS 1, suggesting that the bright infrared ridge of IRS 1 arises from irradiation of the eastern side of the condensation surface by IRS 2.

(3) The high-resolution $C^{18}O$ image shows a velocity gradient of gas toward Source A, which can be interpreted as the rotation, although there is no robust evidence for directly tracing the Keplerian motion of Source A. The infall motion of gas is an alternative way to interpret the velocity gradient.

(4) The ALMA $^{12}CO$ data detected molecular outflows associated with Source A and Source B. The outflows have high velocities of ∼30–70 km s$^{-1}$ and large mass outflow rates of $\sim 10^{-4}\,M_\odot\,\mathrm{yr}^{-1}$ for Source A and $\sim 10^{-3}\,M_\odot\,\mathrm{yr}^{-1}$ for Source B. The derived values correspond to those expected for massive star formation models. The short dynamical timescales of the outflows, less than 1000 yr, suggest that the protostars in Source A and Source B may be massive stars in the creation stage.

(5) Despite the large $\dot{M}_{\mathrm{lobe}}$ which implies large $\dot{M}_{\mathrm{acc}}$ for Source A and Source B, no significant excess was observed in the two sources at the near- and mid-infrared wavelengths. One idea is attenuation of the emission by dust in Source A and Source B. Another idea is the episodic accretion scenario, in which protostars spend most of their time in the quiescent phase, interspersed with short accretion bursts. We discussed the formation scenario of the filamentary structures and massive condensations in RCW 38, and eliminated the possibility of gas compression by the feedback from nearby O stars. A collision between two molecular clouds may have triggered the formation of the filamentary structures in which the massive condensations were formed.

## Acknowledgment

This paper makes use of the following ALMA data: ADS/JAO.ALMA#2015.1.01134.S. ALMA is a partnership of ESO (representing its member states), NSF (USA) and NINS (Japan), together with NRC (Canada), MOST and ASIAA (Taiwan), and KASI (Republic of Korea), in cooperation with the Republic of Chile. The Joint ALMA Observatory is operated by ESO, AUI/NRAO and NAOJ. The authors thank Dr. Takashi Hosokawa for a valuable discussion. This work was financially supported by Grants-in-Aid for Scientific Research (KAKENHI) of the Japanese society for the Promotion of Science (JSPS; grant numbers 18H05440, 18K13582, 15K17607, 15H05694, 24224005, and 26247026), and NAOJ ALMA Scientific Research Grant Number 2016-03B. We thank the anonymous referee for helpful comments, which significantly improved the manuscript.

## References

Anderson, L. D., et al. 2012, A&A, 542, A10
André, P., et al. 2016, A&A, 592, A54
Ascenso, J. 2018, The Birth of Star Clusters (Cham: Springer), 1
Beuther, H., Schilke, P., Sridharan, T. K., Menten, K. M., Walmsley, C. M., & Wyrowski, F. 2002, A&A, 383, 892
Beuther, H., Walsh, A. J., Johnston, K. G., Henning, T., Kuiper, R., Longmore, S. N., & Walmsley, C. M. 2017, A&A, 603, A10
Bolatto, A. D., Wolfire, M., & Leroy, A. K. 2013, ARA&A, 51, 207
Bonnell, I. A., Bate, M. R., Clarke, C. J., & Pringle, J. E. 2001, MNRAS, 323, 785
Caselli, P., et al. 2019, ApJ, 874, 89
Cesaroni, R., et al. 2017, A&A, 602, A59
DeRose, K. L., Bourke, T. L., Gutermuth, R. A., Wolk, S. J., Megeath, S. T., Alves, J., & Nürnberger, D. 2009, AJ, 138, 33
Dunham, M. M., et al. 2016, ApJ, 823, 160
Dunham, M. M., & Vorobyov, E. I. 2012, ApJ, 747, 52
Elmegreen, B. G., & Lada, C. J. 1977, ApJ, 214, 725
Frerking, M. A., Langer, W. D., & Wilson, R. W. 1982, ApJ, 262, 590

Fukui, Y., et al. 2016, ApJ, 820, 26
Fukui, Y., et al. 2018, ApJ, 859, 166
Fukui, Y., et al. 2019, ApJ, 886, 14
Fukui, Y., Habe, A., Inoue, T., Enokiya, R., & Tachihara, K. 2021a, PASJ, 73, S1
Fukui, Y., Inoue, T., Hayakawa, T., & Torii, K. 2021b, PASJ, 73, S21
Furniss, I., Jennings, R. E., & Moorwood, A. F. M. 1975, ApJ, 202, 400
Guzmán, A. E., et al. 2014, ApJ, 796, 117
Hirota, T., Machida, M. N., Matsushita, Y., Motogi, K., Matsumoto, N., Kim, M. K., Burns, R. A., & Honma, M. 2017, Nature Astron., 1, 0146
Hosokawa, T., Hirano, S., Kuiper, R., Yorke, H. W., Omukai, K., & Yoshida, N. 2016, ApJ, 824, 119
Hosokawa, T., & Inutsuka, S. 2006, ApJ, 646, 240
Hosokawa, T., & Omukai, K. 2009, ApJ, 691, 823
Hosokawa, T., Yorke, H. W., & Omukai, K. 2010, ApJ, 721, 478
Huchtmeier, W. 1974, A&A, 32, 335
Inoue, T., & Fukui, Y. 2013, ApJ, 774, L31
Inoue, T., Hennebelle, P., Fukui, Y., Matsumoto, T., Iwasaki, K., & Inutsuka, S. 2018, PASJ, 70, S53
Izumi, N., et al. 2021, PASJ, 73, 174
Johnston, K. G., et al. 2015, ApJ, 813, L19
Krumholz, M. R., Cunningham, A. J., Klein, R. I., & McKee, C. F. 2010, ApJ, 713, 1120
Krumholz, M. R., Klein, R. I., & McKee, C. F. 2007, ApJ, 656, 959
Krumholz, M. R., Klein, R. I., & McKee, C. F. 2012, ApJ, 754, 71
Krumholz, M. R., Klein, R. I., McKee, C. F., Offner, S. S. R., & Cunningham, A. J. 2009, Science, 323, 754
Kuhn, M. A., Getman, K. V., & Feigelson, E. D. 2015, ApJ, 802, 60
Kuiper, R., & Hosokawa, T. 2018, A&A, 616, A101
Kuiper, R., Klahr, H., Beuther, H., & Henning, T. 2010, ApJ, 722, 1556
Kuiper, R., Klahr, H., Beuther, H., & Henning, T. 2011, ApJ, 732, 20
Leung, C. M., Herbst, E., & Huebner, W. F. 1984, ApJS, 56, 231
McKee, C. F., & Tan, J. C. 2003, ApJ, 585, 850
MacLaren, I., Richardson, K. M., & Wolfendale, A. W. 1988, ApJ, 333, 821
McMullin, J. P., Waters, B., Schiebel, D., Young, W., & Golap, K. 2007, in ASP Conf. Ser., 376, Astronomical Data Analysis Software and Systems XVI, ed. R. A. Shaw et al. (San Francisco: ASP), 127
Matsushita, Y., Takahashi, S., Machida, M. N., & Tomisaka, K. 2019, ApJ, 871, 221
Maud, L. T., Moore, T. J. T., Lumsden, S. L., Mottram, J. C., Urquhart, J. S., & Hoare, M. G. 2015, MNRAS, 453, 645
Meyer, D. M. A., Kuiper, R., Kley, W., Johnston, K. G., & Vorobyov, E. 2018, MNRAS, 473, 3615
Meyer, D. M. A., Vorobyov, E. I., Kuiper, R., & Kley, W. 2017, MNRAS, 464, L90
Motogi, K., et al. 2017, ApJ, 849, 23
Motogi, K., Hirota, T., Machida, M. N., Yonekura, Y., Honma, M., Takakuwa, S., & Matsushita, S. 2019, ApJ, 877, L25
Motte, F., et al. 2018, Nature Astron., 2, 478
Myers, P. C. 2009, ApJ, 700, 1609
Nakano, T. 1989, ApJ, 345, 464
Offner, S. S. R., Lee, E. J., Goodman, A. A., & Arce, H. 2011, ApJ, 743, 91
Ohashi, N., et al. 2014, ApJ, 796, 131
Ohashi, S., Sanhueza, P., Chen, H.-R. V., Zhang, Q., Busquet, G., Nakamura, F., Palau, A., & Tatematsu, K. 2016, ApJ, 833, 209
Ohashi, S., Sanhueza, P., Sakai, N., Kand ori, R., Choi, M., Hirota, T., Nguyen-Luong, Q., & Tatematsu, K. 2018, ApJ, 856, 147
Onishi, T., Mizuno, A., Kawamura, A., Tachihara, K., & Fukui, Y. 2002, ApJ, 575, 950
Ossenkopf, V., & Henning, T. 1994, A&A, 291, 943
Peters, T., Banerjee, R., Klessen, R. S., Mac Low, M.-M., Galván-Madrid, R., & Keto, E. R. 2010, ApJ, 711, 1017
Sánchez-Monge, Á., et al. 2013, A&A, 552, L10
Shima, K., Tasker, E. J., & Habe, A. 2017, MNRAS, 467, 512
Stahler, S. W., Palla, F., & Salpeter, E. E. 1986, ApJ, 302, 590
Spaans, M., & van Dishoeck, E. F. 1997, A&A, 323, 953
Tachihara, K., Fukui, Y., Hayakawa, T., & Inoue, T. 2018, arXiv:1811.02224
Tachihara, K., Onishi, T., Mizuno, A., & Fukui, Y. 2002, A&A, 385, 909
Tan, J. C., Beltran, M. T., Caselli, P., Fontani, F., Fuente, A., Krumholz, M. R., McKee, C. F., & Stolte, A. 2014, in Protostars and Planets VI, ed. H. Beuther et al. (Tuscon: University Arizona Press), 149
Tokuda, K., et al. 2014, ApJ, 789, L4
Tokuda, K., et al. 2016, ApJ, 826, 26
Tokuda, K., et al. 2019a, ApJ, 886, 15
Tokuda, K., et al. 2019b, PASJ, 71, 73
Tokuda, K., et al. 2020, ApJ, 899, 10
Torii, K., et al. 2011, ApJ, 738, 46
Torii, K., et al. 2015, ApJ, 806, 7
Torii, K., et al. 2017a, ApJ, 835, 142
Torii, K., et al. 2017b, ApJ, 840, 111
Vigil, M. 2004, Master thesis, Massachusetts Institute of Technology
Wang, P., Li, Z.-Y., Abel, T., & Nakamura, F. 2010, ApJ, 709, 27
Williams, J. P., de Geus, E. J., & Blitz, L. 1994, ApJ, 428, 693
Wilson, T. L., & Rood, R. 1994, ARA&A, 32, 191
Winston, E., Wolk, S. J., Bourke, T. L., Megeath, S. T., Gutermuth, R., & Spitzbart, B. 2011, ApJ, 743, 166
Wolfire, M. G., & Cassinelli, J. P. 1986, ApJ, 310, 207
Wolk, S. J., Bourke, T. L., & Vigil, M. 2008, in Handbook of Star-Forming Regions, Vol. II, ed. B. Reipurth (San Francisco: ASP), 124
Wolk, S. J., Spitzbart, B. D., Bourke, T. L., & Alves, J. 2006, AJ, 132, 1100
Zhang, Y., et al. 2019, ApJ, 873, 73